Large-Area Organic−Transition Metal Dichalcogenide Hybrid Light-Emitting Device

Jongchan Kim, Siwei Zhang, Shaocong Hou, Byungjun Lee, Guodan Wei, and Stephen R. Forrest*

ACCESS | Metrics & More | Article Recommendations | Supporting Information

ABSTRACT: We demonstrate a hybrid light-emitting device (LED) employing a chemical-vapor-deposition grown, centimeter-scale monolayer of WS_2 (mWS_2) as the active luminescent material embedded within conductive organic layers. The active area of the hybrid LED is composed of mWS_2, located within the organic host matrix, sandwiched between the hole- and electron-transporting organic layers. The mWS_2 shows fast exciton decay and efficient light outcoupling compared to the organic dyes used for OLEDs, whereas organic layers enable a precisely controlled, large-area fabrication process. As a result, LEDs with an average external quantum efficiency of $0.3 \pm 0.3\%$ and with the highest efficiency of 1% were achieved. Also, we show that negatively charged excitons, also known as trions, are generated in the mWS_2 with the injected current, causing an efficiency roll-off at high current densities. Our result introduces a means for incorporating a range of emissive inorganic thin films into an organic device structure, thereby taking advantage of the positive attributes of both material systems.

KEYWORDS: *2D material, organic, LED, transition metal dichalcogenide, large area*
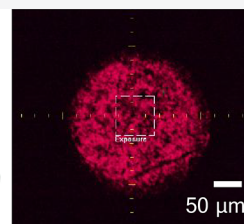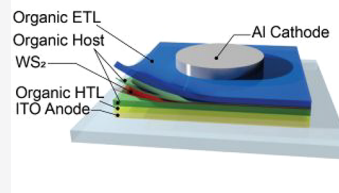
I. INTRODUCTION

Two-dimensional (2D) layered materials show unusual physical properties that range from those of a wide-bandgap insulator to a semiconductor, a semimetal, or metal.[1] Monolayer transition metal dichalcogenides (TMDCs), a subclass of 2D layered materials, have promising optical characteristics such as efficient photoluminescence (PL),[2,3] fast exciton decay,[4] and high chemical and air stability.[5] As a result, TMDCs have been used in various optoelectronic devices, showing distinct characteristics from conventional bulk semiconductors.[6−14] For example, light-emitting devices (LEDs) based on hexagonal boron nitride (h-BN) insulators combined with TMDCs as the active luminescent materials have been demonstrated.[10−13,15] However, the LEDs require a sequence of complex layer transfers during the fabrication and are constrained by the limited size of the 2D semiconductor flakes (several μm).[11,13] Recently, a large-area TMDC-based LED has been demonstrated, although its external quantum efficiency was low ($\sim 10^{-4}\%$) compared to LEDs based on exfoliated TMDCs.[16,17]

Here, we demonstrate centimeter-scale LEDs using a monolayer of red-emitting WS_2 (mWS_2) embedded within organic transport and host layers with an efficiency comparable to much smaller, exfoliated-TMDC-based LEDs. The organic layers enable simplified deposition and precise placement of the TMDC within the structure to optimize the device characteristics. We transfer a 1 cm^2, chemical-vapor-deposition (CVD) grown mWS_2 onto a predeposited organic stack of the 4,4′-bis(N-carbazolyl)-1,1′-biphenyl (CBP) host/4,4′-cyclo-

hexylidenebis-*N,N*-bis(4-methylphenyl)benzenamine (TAPC) hole transport layer/MoO_x hole injection layer/indium tin oxide (ITO) anode. This is followed by deposition of the remainder of the host layer, thereby burying the mWS_2. The device is completed with a 4,6-bis(3,5-di(pyridin-3-yl)phenyl)-2-methylpyrimidine (B3PYMPM) electron transport layer and an Al cathode. Embedding a monolayer TMDC within the host enables efficient radiative emission via Förster transfer of excitons from the organic layers, while separating the TMDC from the heterointerface to avoid quenching at the heterointerface, especially at high current densities.[18,19] The LEDs show an average external quantum efficiency of $0.3 \pm 0.3\%$, with the highest value of 1%.

II. RESULTS

Figure 1a shows the structure of the hybrid LED with the frontier energy levels in Figure 1b. Organic hole injection/transport layers (HIL and HTL) comprising 2 nm thick MoO_3 and 50 nm thick TAPC are deposited on top of the transparent anode (150 nm thick ITO), and then an organic host layer comprising 12 nm thick neat CBP is deposited. An mWS_2 is transferred onto the organic host by the method described in
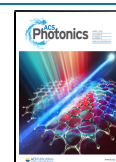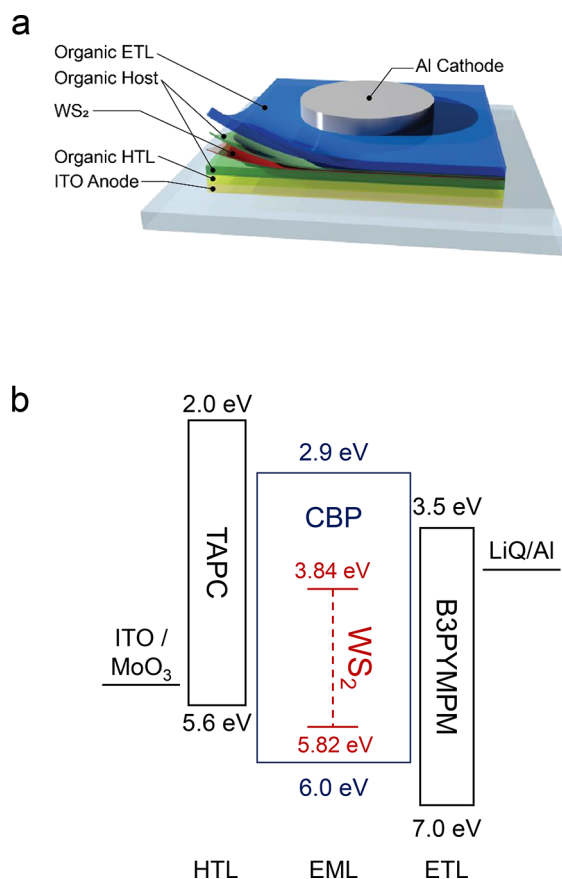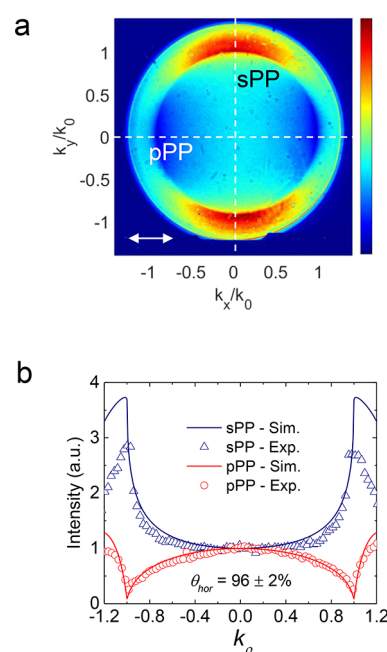
Figure 1. Hybrid 2D-organic LED. (a) Schematic illustration of the hybrid LED comprising a monolayer WS$_2$ active layer sandwiched between organic conducting and exciton-generating layers. (b) Frontier orbital energy diagram of the materials used in the LED.

Figure 2. TDM orientation of monolayer WS$_2$ in a CBP host matrix. (a) Measured Fourier plane imaging microscopy polar plots for the monolayer WS$_2$ in the CBP host matrix. (b) Intensity profiles of the polar plot in the pPP and sPP planes (data points) along with the simulated fits (solid lines).

the Supporting Information, Figure S1. After transfer, we deposit a 3 nm thick capping host (CBP) layer, 55 nm electron transport layer (ETL), and the top Al contact.

The percentage of transition dipole moments (TDMs), θ_{hor}, of the mWS$_2$ in the CBP host aligned parallel to the substrate plane is measured via Fourier plane imaging microscopy (FIM).[20−24] When θ_{hor} = 100%, all TDMs are oriented parallel to the substrate, θ_{hor} = 67% for random, and θ_{hor} = 0% for a perfect vertical alignment. Figure 2a shows the polar emission pattern obtained from the mWS$_2$ embedded within the CBP host matrix measured by FIM. The intensity profiles (data points) in the p-polarized plane (pPP) and s-polarized plane (sPP) are fit to theory (solid line) in Figure 2b, as described in ref 15. The data show θ_{hor} = 96 ± 2%, corresponding to near-perfect horizontal orientation of the mWS$_2$ TDM. This leads to an exceptionally high light outcoupling efficiency of the LED, as shown in Figure S2.[25,26]

The optimal position of the mWS$_2$ within the emission layer is determined by measuring the exciton density profile. To do this, we deposit an ultrathin (0.5 Å) layer of the phosphor Pt-octaethylporphyrin (PtOEP) at 2.5 nm intervals in a series of devices, starting from the HTL/emissive layer (EML) interface, to the EML/electron transport layer (ETL) interface (see Figure 3a). The frontier energy levels of PtOEP align with those of mWS$_2$. Hence, the emission intensity from the PtOEP at a fixed current density (J) is proportional to the exciton density at its location. The measured exciton density profiles for various J are shown in Figure 3b, with the peak near the

EML/ETL interface. The peak position changes from x = 15 to 12.5 nm at J = 100 mA/cm^2 due to increased exciton quenching near the heterointerface at high J. Figure 3c shows the external quantum efficiency (EQE) of each sensing layer sample, showing a decreasing efficiency as the sensing layer moves farther from the interface due to the reduced exciton density. The measured spectra of the samples are shown in Figure 3d. We conclude from these data that the mWS$_2$ should be positioned ∼3 nm away from the EML/ETL interface to enable harvesting of the highest density of excitons while limiting exciton quenching.

With the structural design in Figure 3, a hybrid LED was fabricated following the procedure in Figure S1, with the performance given in Figure 4. Figure 4a shows EQE vs J, with an average peak EQE = 0.3 ± 0.3%, and the highest efficiency device with EQE = 1%. The inset shows the image of an array of 0.2 mm^2 devices. Figure 4b shows the $J−V$ characteristics with a microscopic image of the device electroluminescence in the inset. The electroluminescence spectra at various J are shown in Figure 4c, exhibiting a pronounced hypsochromic shift with current in the device. Note that the EQE in Figure 4a increases with current at J < 0.01 mA/cm^2. As shown in Figure 4b, the device shows a noticeable leakage current at V < 2.5 V, causing a significant quantity of charges to be lost rather than generate excitons. Thus, as the injected current surpasses the leakage current, EQE also increases.

Figure 5a and b show the photoluminescence of the mWS$_2$ embedded within electron- and hole-only devices (EOD and HOD, respectively) at several current densities. The device structure and $J−V$ characteristics of the EOD and HOD are included in Figure S3. There is a pronounced hypsochromic mWS$_2$ photoluminescence peak shift with current in the EOD, which is absent in the HOD. We conclude that injected electrons in the EOD combine with the generated excitons to form negatively charged excitons, or trions.[27,28] The binding
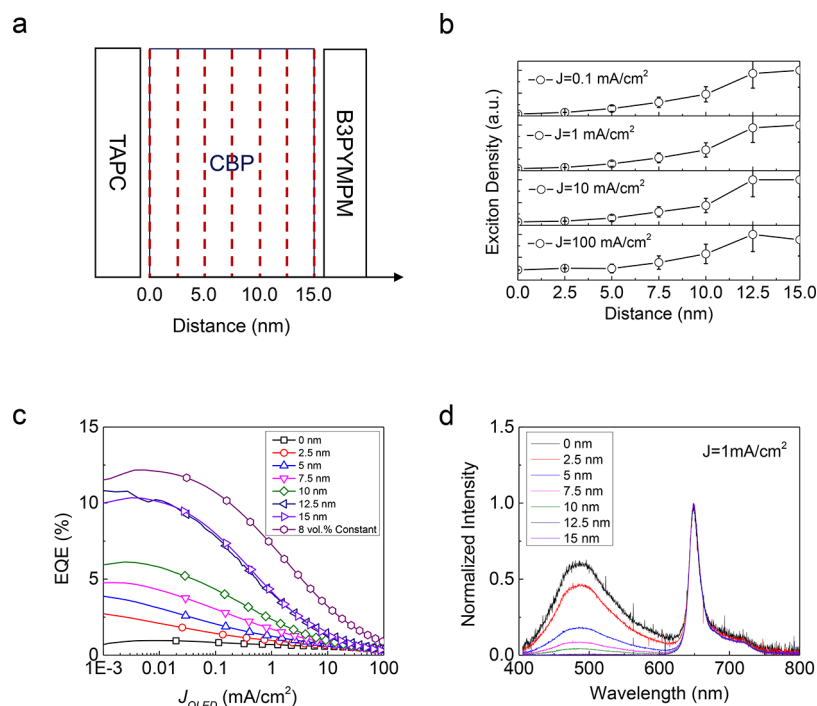
Figure 3. Exciton density profiles in the EML. (a) Illustration showing the placement of the PtOEP MSLs within the emissive layer. (b) Measured exciton density profile at different current densities. (c) J−EQE characteristics of the samples with the sensing layer at each different position. (d) Electroluminescence spectrum of samples with the sensing layer at different positions at J = 1 mA/cm^2.

energy of trions has previously been shown to be 20−30 meV relative to the neutral exciton,[27,29] a value that corresponds to the energy shift in Figure 5a. The absence of a peak shift of the mWS$_2$ photoluminescence in the HOD is due to the asymmetric charge trapping in the CBP−mWS$_2$−CBP quantum well structure. The energy barrier for electrons at the CBP LUMO-mWS$_2$ conduction band discontinuity (see Figure 1b) is larger than the barrier at the CBP HOMO-mWS$_2$ valence band discontinuity for holes.[30] As a result, hole trions do not form as efficiently as electron trions, thus showing no apparent peak shift in Figure 5b.

III. DISCUSSION

The introduction of an inorganic active layer into an OLED structure using dry transfer enables a variety of material selections to be combined with organic thin films in a hybrid LED. Using an organic host matrix separates charge conduction from the guest emission processes, allowing for optimization of each material to serve its intended purpose. Excitons are efficiently formed in the conductive host layer and then transferred to the luminescent active material (mWS$_2$), which is positioned near the maximum exciton density within the Förster radius, as determined from the sensing layer experiments in Section II.

The use of a host matrix differentiates the device structure from the previously reported TMDC LEDs,[15,16] where the TMDCs are located directly between the hole- and electron-transport layers. However, according to Giebink et al.[18] and Wang et al.,[19] the heterointerface is prone to charge/exciton accumulation and the coexistence of a high density of excitons and charges result in degradation of the active material or even morphological instabilities.[31] The use of a host matrix enables placing the TMDC apart from the heterointerface with benefits to device stability.

CVD-grown mWS$_2$ has a high defect density comprising S vacancies formed during the growth process, limiting the device efficiency. Also, cracks and holes are generated during the dry transfer since mWS$_2$ is a polycrystal bound by weak van der Waals forces.[32] The S vacancies lead to emission from the defect levels in both the EOD and HOD, even when no charges are injected, as shown in Figure 5c.[33,34] The physical defects lead to the EQE varying by orders of magnitude even within the same growth run. The defects are nonradiative, appearing as the dark spots on the device emitting surface, as shown by the image in Figure 4b, inset.

The electroluminescence spectra show emission from mWS$_2$ but not from the organic host in Figure 4c, demonstrating efficient Förster transfer of the excitons generated at the EML/ETL interface, into mWS$_2$. The spectrum shows a bathochromic shift depending on the drive current. In Figure 5c, the photoluminescence of mWS$_2$ in the EOD, excited with a 532 nm laser, is shown as a function of current density, with the deconvolution of the spectrum using two Lorentzians with exciton and trion emission peaks at wavelengths of λ = 617 and 628 nm, respectively.[33] The trion peak intensity increases with the current density, as expected. The laser selectively excites A excitons of mWS$_2$ ($\sim$2.0 eV), but not the higher energy ($\sim$2.4 eV) B excitons, allowing us to not consider their spectra in the peak fits.[35] The ratio between the emission intensity of excitons and the increased emission intensity of trions due to the charge injection is found using the law of mass action:[28,36,37]

$$\frac{N_X n_{el}}{N_{X^-}} = \left(\frac{4 \mu_X m_e}{\pi \hbar^2 \mu_{X^-}} \right) k_B T \, \exp\left(-\frac{E_B}{k_B T} \right) \tag{1}$$

where N_X, N_{X^-}, and n_{el} are the concentrations of excitons, trions, and electrons, with respective masses of μ_X, μ_{X^-}, and m_e,[38] k_B is the Boltzmann coefficient, T is the temperature, and
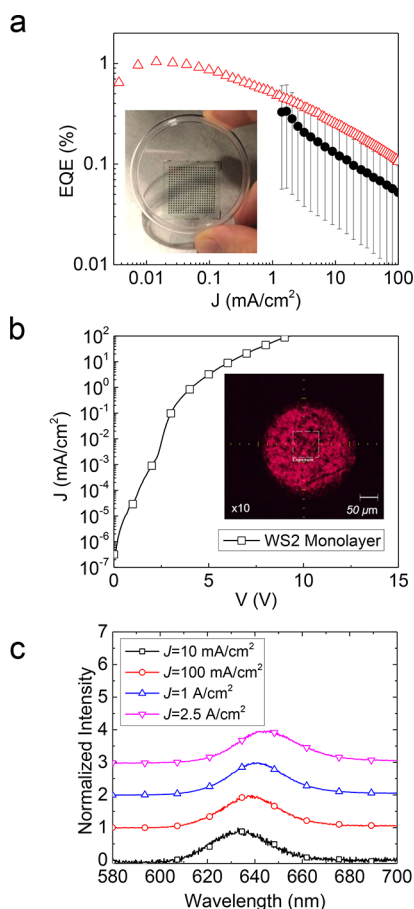
Figure 4. Performance characteristics of the hybrid LED. (a) J−EQE characteristics of the hybrid LEDs. The average and the highest EQE data are shown in black and red data points, respectively. Inset: Photograph of the LEDs grown on a 2.5 × 2.5 cm² glass substrate. (b) J−V characteristics of the hybrid LED. Inset: Photograph of the device electroluminescence. The diameter of the device is 250 μm. (c) Current-dependent electroluminescence spectra of the hybrid LED.

E_B is the trion biding energy (20 meV).[27] The reduced masses of electron trions and exciton are $\mu_X^{-1} = 2m_e^{-1} + m_h^{-1}$ and $\mu_X^{-1} = m_e^{-1} + m_h^{-1}$. Equation 1 describes the ratio between the concentrations of excitons (N_X) and trions (N_{X-}) in the presence of an electron concentration. It is apparent that the change of N_X/N_{X-} is dependent on n_{el} within the mWS$_2$ film. The change of N_X/N_{X^-} is determined from the relative emission intensities of trions and excitons vs J, which correspond to $\gamma_{tr}N_{X^-}$ and $\gamma_{ex}N_X$ where γ_{tr} and γ_{ex} are the intensity of each particle, which is described as[36]

$$\frac{I_{X^-}}{I_{total}} = \frac{\gamma_{tr}N_{X^-}}{\gamma_{ex}N_X + \gamma_{tr}N_{X^-}} = \frac{\gamma_{tr}}{\gamma_{ex}}\frac{N_{X^-}}{N_X} \bigg/ \left(1 + \frac{\gamma_{tr}}{\gamma_{ex}}\frac{N_{X^-}}{N_X}\right) \quad (2)$$

where γ_{tr} and γ_{ex} were obtained from fitting parameters in rate equations by Peimyoo et al.[38] Equation 2 yields the relation between the injected current density (n_{el}) and the amount of increased spectral weight of trions vs electron density as shown in Figure 5d. The theoretical fit and the measured data are in close correspondence, showing that the bathochromic shift of the electroluminescence occurs due to electron trion emission.

In addition to the spectral shift, the radiative decay rate of trions is 5 times less than that of the excitons,[38] resulting in a reduction in mWS$_2$ photoluminescence intensity as a function of injected electron density in Figure 5a. Therefore, the high electron density causes a decreased internal quantum efficiency of mWS$_2$ and a corresponding roll-off in EQE at $J > 0.01$ mA/cm² (Figure 4a). As a result, placing mWS$_2$ in the region with reduced electron density while maintaining high exciton density enables efficient EQE with reduced roll-off.

IV. CONCLUSIONS

We demonstrated a light-emitting device with an active layer comprising a CVD-grown, large-area mWS$_2$ as the luminescent material, combined with organic buffer layers (charge-transport and host matrix layers) that enable efficient charge transport and exciton generation. The use of an mWS$_2$ enables principally horizontally aligned transition dipole moments and fast exciton decay, leading to an enhanced outcoupling and device stability. Moreover, the organic host was used to efficiently generate and inject excitons into the mWS$_2$ via Förster transfer. Thus, the mWS$_2$ was positioned several nanometers distant from the heterointerface, which prevents sites for nonradiative recombination. LEDs with diameters of 250 μm exhibited average EQE = 0.3 ± 0.3% with a peak of 1%. In addition, electron- and hole-only devices indicated that the injected electrons in mWS$_2$ combine with excitons, generating trions, reducing EQE at high current densities. Our results show an efficient way of incorporating promising luminescent materials into the organic device structure.

V. METHODS

Device Fabrication. OLEDs were grown on glass substrates with a predeposited and patterned 150 nm thick ITO anode (Thin Film Devices, Inc.). The ITO-coated substrates were treated in a UV-ozone chamber for 15 min prior to organic film deposition. The organic film layers comprising CBP 12 nm/TAPC 50 nm/MoO$_3$ 2 nm were grown by vacuum thermal evaporation (VTE) in a chamber with a base pressure of 1×10^{-7} Torr. The mWS$_2$ was dry-transferred onto the CBP surface following the procedure described in Figure S1. After transfer, the sample was left in the VTE chamber for 2 h. The device was completed by depositing 100 nm Al/1.5 nm LiQ/55 nm B3PYMPM/3 nm CBP on top of the mWS$_2$.

Dry Transfer Process. The CVD-grown monolayer WS$_2$ on a SiO$_2$ substrate was purchased from 6Carbon Technology. An mWS$_2$ deposited on a SiO$_2$/Si substrate (CVD grown) is immersed in a 100 mL solution comprising bis-(trifluoromethane)sulfonimide (TFSI)/dichloroethane (DCE) (0.2 mg/mL). It is heated for 50 min at 100 °C,[39] as shown in step A, Figure S1. After the TFSI treatment, the sample surface is dried in N$_2$. A polydimethylsiloxane (PDMS) handle is attached to the mWS$_2$ as shown in steps B and C. The PDMS attached to the Si substrate is immersed into a KOH etchant solution (14 g of KOH in 200 mL of DI water) at 60 °C. Once the substrate falls away, the mWS$_2$ attached to PDMS (step E) is once more dried in N$_2$. The mWS$_2$ on PDMS is pressed gently onto the organic surface using an automated transfer stage, and the PDMS is peeled off, leaving the mWS$_2$ on the organic surface (step F).

Device Characterization. The voltage−current density−EQE characteristics of the LEDs were measured using a parameter analyzer (HP4145, Hewlett-Packard) and a calibrated photodiode (S3584-08, Hamamatsu Photonics) following standard procedures.[40] The emission spectra were
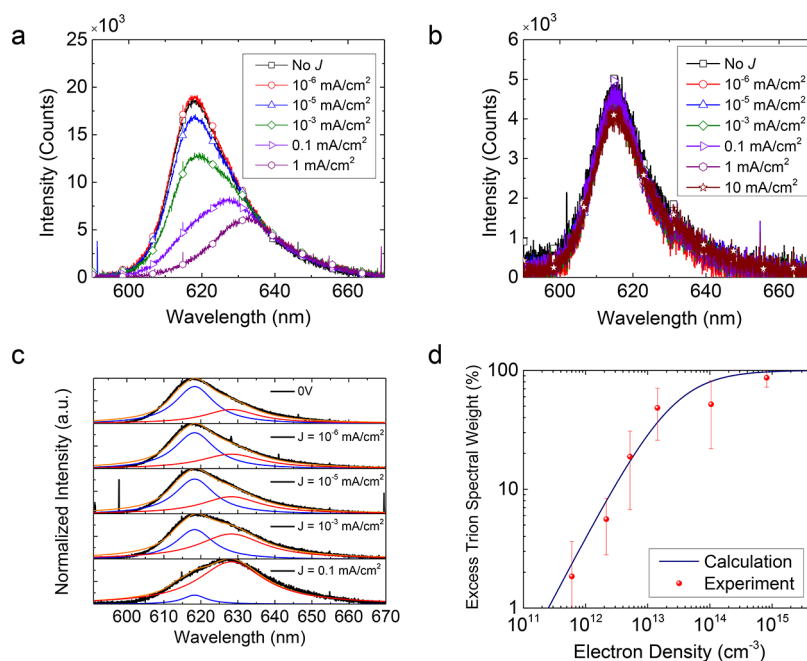
Figure 5. Photoluminescence of monolayer WS$_2$ embedded in a single-charge device. (a, b) Photoluminescence of a monolayer WS$_2$ within the (a) electron- and (b) hole-only device with varied injection current. (c) Photoluminescence of mWS$_2$ in the electron-only device as a function of current density with the deconvolution of the spectrum using two Lorentzians with exciton and trion emission peaks. The blue, red, and orange lines show the exciton, trion, and the summed total spectrum, respectively, from the fits. (d) Increased spectral weight of trions compared with the total emission from excitons and trions, as a function of the injected electron density (n_{el}).

measured using a calibrated spectrometer (USB4000, Ocean Optics, Inc.) connected to the device via an optical fiber (P400-5-UV−vis, Ocean Optics, Inc.).

Transition Dipole Moment Measurement. The orientation of the TDM of the mWS$_2$ was measured using Fourier plane imaging microscopy following previously reported procedures.[21]

Electron- and Hole-Only Device Photoluminescence Spectral Fitting. The photoluminescence spectrum of mWS$_2$ in the EOD was fit using two Lorentzian curves following

$$f(\lambda) = \frac{A\gamma^2}{(\lambda - \lambda_0)^2 + \gamma^2} \tag{3}$$

at center wavelengths of $\lambda_0 = 617$ and 628 nm, where γ is the half-width at half-maximum and A is the constant for the peak height. A least-squares algorithm was used to fit the measured photoluminescence data with the two Lorentzian curves.

Exciton Formation Analysis. The exciton density at the position x, $N(x)$, was mapped across the emissive layer using the sensing layer method.[41,42] Ultrathin ($\sim$1 Å) red phosphorescent (PtOEP) layers were deposited at locations shown in Figure 3a in a series of otherwise identical OLEDs. The emission spectrum from the PtOEP sensing layer from each position (x) and the CBP organic host is

$$I_{total}(\lambda, x) = a_{PtOEP}(x) I_{PtOEP}(\lambda) + a_{CBP}(x) I_{CBP}(\lambda) \tag{4}$$

where $I_{total}(\lambda, x)$ is the total emission spectrum comprising the spectra of PtOEP ($I_{PtOEP}(\lambda)$) and the CBP host matrix ($I_{CBP}(\lambda)$), with the relative weights of $a_{PtOEP}(x)$ and $a_{CBP}(x)$, respectively. Then, the outcoupled exciton density at position x, $N(x)\,\eta_{out}(x)$, becomes

$$N(x)\,\eta_{out}(x) = \frac{J_0}{q}\eta_{EQE}(x)$$

$$\times \frac{a_{PtOEP}(x)\int I_{PtOEP}(\lambda)/\lambda\;d\lambda}{a_{PtOEP}(x)\int I_{PtOEP}(\lambda)/\lambda\;d\lambda + a_{CBP}(x)\int I_{CBP}(\lambda)/\lambda\;d\lambda} \tag{5}$$

where J_0 is the current density and $\eta_{out}(x)$ and $\eta_{EQE}(x)$ are the outcoupling and external quantum efficiencies of the sensing layer at position x. The $\eta_{out}(x)$ is calculated based on Green's function analysis[43] in Figure S4. The range of $\sim$3 nm[42] Förster energy transfer limits the spatial resolution of the measurement.

■ ASSOCIATED CONTENT

ⓈⒾ Supporting Information

The Supporting Information is available free of charge at https://pubs.acs.org/doi/10.1021/acsphotonics.1c00047.

> Detailed schematic illustration of the dry transfer process of the monolayer WS$_2$, calculated distribution of the emitted light power of the OLED structure into different optical modes, with respect to the varied TDM orientation, structures and the $J-V$ characteristics of the hole- and electron-only devices in Figure 5, and the calculated outcoupling efficiency of the sensing layers at various locations in the emissive layer in Figure 3a (PDF)

■ AUTHOR INFORMATION

Corresponding Author

  Stephen R. Forrest − *Department of Electrical and Computer Engineering, Department of Physics, and Department of Materials Science and Engineering, University of Michigan,*

Ann Arbor, Michigan 48109, United States; ● orcid.org/ 0000-0003-0131-1903; Email: stevefor@umich.edu

Authors

Jongchan Kim − *Department of Electrical and Computer Engineering, University of Michigan, Ann Arbor, Michigan 48109, United States*

Siwei Zhang − *Department of Physics, Tsinghua-Berkeley Shenzhen Institute, Shenzhen 518055, China*

Shaocong Hou − *Department of Electrical and Computer Engineering, University of Michigan, Ann Arbor, Michigan 48109, United States*

Byungjun Lee − *Department of Electrical and Computer Engineering, University of Michigan, Ann Arbor, Michigan 48109, United States*

Guodan Wei − *Department of Physics, Tsinghua-Berkeley Shenzhen Institute, Shenzhen 518055, China*

Complete contact information is available at:
https://pubs.acs.org/10.1021/acsphotonics.1c00047

Notes

The authors declare the following competing financial interest(s): One of the authors (SRF) has an equity interest in one of the sponsors of this research (UDC). This apparent conflict of interest is under management by the University of Michigan Office of Research.

◼ REFERENCES

(1) Castellanos-Gomez, A. Why All the Fuss about 2D Semiconductors? *Nat. Photonics* **2016**, *10*, 202−204.

(2) Amani, M.; Burke, R. A.; Ji, X.; Zhao, P.; Lien, D.-H.; Taheri, P.; Ahn, G. H.; Kirya, D.; Ager, J. W.; Yablonovitch, E.; Kong, J.; Dubey, M.; Javey, A. High Luminescence Efficiency in MoS₂ Grown by Chemical Vapor Deposition. *ACS Nano* **2016**, *10* (7), 6535−6541.

(3) Kim, H.; Lien, D.-H.; Amani, M.; Ager, J. W.; Javey, A. A Highly Stable Near-Unity Photoluminescence Yield in Monolayer MoS₂ by Fluoropolymer Encapsulation and Superacid Treatment. *ACS Nano* **2017**, *11* (5), 5179−5185.

(4) Palummo, M.; Bernardi, M.; Grossman, J. C. Exciton Radiative Lifetimes in Two-Dimensional Transition Metal Dichalcogenides. *Nano Lett.* **2015**, *15* (5), 2794−2800.

(5) Novoselov, K. S.; Mishchenko, A.; Carvalho, A.; Castro Neto, A. H. 2D Materials and van Der Waals Heterostructures. *Science* **2016**, *353* (6298), aac9439.

(6) Wang, J.; Verzhbitskiy, I.; Eda, G. Electroluminescent Devices Based on 2D Semiconducting Transition Metal Dichalcogenides. *Adv. Mater.* **2018**, *30* (47), 1802687.

(7) Zhou, X.; Hu, X.; Yu, J.; Liu, S.; Shu, Z.; Zhang, Q.; Li, H.; Ma, Y.; Xu, H.; Zhai, T. 2D Layered Material-Based van Der Waals Heterostructures for Optoelectronics. *Adv. Funct. Mater.* **2018**, *28* (14), 1706587.

(8) Wang, C.; Yang, F.; Gao, Y. The Highly-Efficient Light-Emitting Diodes Based on Transition Metal Dichalcogenides: From Architecture to Performance. *Nanoscale Adv.* **2020**, *2* (10), 4323−4340.

(9) Baugher, B. W. H.; Churchill, H. O. H.; Yang, Y.; Jarillo-Herrero, P. Optoelectronic Devices Based on Electrically Tunable p-n Diodes in a Monolayer Dichalcogenide. *Nat. Nanotechnol.* **2014**, *9* (4), 262−267.

(10) Zhang, Y. J.; Oka, T.; Suzuki, R.; Ye, J. T.; Iwasa, Y. Electrically Switchable Chiral Light-Emitting Transistor. *Science* **2014**, *344* (6185), 725−728.

(11) Withers, F.; Del Pozo-Zamudio, O.; Schwarz, S.; Dufferwiel, S.; Walker, P. M.; Godde, T.; Rooney, A. P.; Gholinia, A.; Woods, C. R.; Blake, P.; Haigh, S. J.; Watanabe, K.; Taniguchi, T.; Aleiner, I. L.; Geim, A. K.; Fal'ko, V. I.; Tartakovskii, A. I.; Novoselov, K. S. WSe₂ Light-Emitting Tunneling Transistors with Enhanced Brightness at Room Temperature. *Nano Lett.* **2015**, *15* (12), 8223−8228.

(12) Yang, W.; Shang, J.; Wang, J.; Shen, X.; Cao, B.; Peimyoo, N.; Zou, C.; Chen, Y.; Wang, Y.; Cong, C.; Huang, W.; Yu, T. Electrically Tunable Valley-Light Emitting Diode (VLED) Based on CVD-Grown Monolayer WS₂. *Nano Lett.* **2016**, *16* (3), 1560−1567.

(13) Gu, J.; Chakraborty, B.; Khatoniar, M.; Menon, V. M. A Room-Temperature Polariton Light-Emitting Diode Based on Monolayer WS₂. *Nat. Nanotechnol.* **2019**, *14* (11), 1024−1028.

(14) Pak, J.; Lee, I.; Cho, K.; Kim, J.-K.; Jeong, H.; Hwang, W.-T.; Ahn, G. H.; Kang, K.; Yu, W. J.; Javey, A.; Chung, S.; Lee, T. Intrinsic Optoelectronic Characteristics of MoS₂ Phototransistors *via* a Fully Transparent van Der Waals Heterostructure. *ACS Nano* **2019**, *13* (8), 9638−9646.

(15) Withers, F.; Del Pozo-Zamudio, O.; Mishchenko, A.; Rooney, A. P.; Gholinia, A.; Watanabe, K.; Taniguchi, T.; Haigh, S. J.; Geim, A. K.; Tartakovskii, A. I.; Novoselov, K. S. Light-Emitting Diodes by Band-Structure Engineering in van Der Waals Heterostructures. *Nat. Mater.* **2015**, *14* (3), 301−306.

(16) Andrzejewski, D.; Myja, H.; Heuken, M.; Grundmann, A.; Kalisch, H.; Vescan, A.; Kümmell, T.; Bacher, G. Scalable Large-Area p-i-n Light-Emitting Diodes Based on WS₂ Monolayers Grown via MOCVD. *ACS Photonics* **2019**, *6* (8), 1832−1839.

(17) Andrzejewski, D.; Oliver, R.; Beckmann, Y.; Grundmann, A.; Heuken, M.; Kalisch, H.; Vescan, A.; Kümmell, T.; Bacher, G. Flexible Large-Area Light-Emitting Devices Based on WS₂ Monolayers. *Adv. Opt. Mater.* **2020**, *8* (20), 2000694.

(18) Giebink, N. C.; D'Andrade, B. W.; Weaver, M. S.; Brown, J. J.; Forrest, S. R. Direct Evidence for Degradation of Polaron Excited States in Organic Light Emitting Diodes. *J. Appl. Phys.* **2009**, *105* (12), 124514.

(19) Wang, Q.; Aziz, H. Degradation of Organic/Organic Interfaces in Organic Light-Emitting Devices Due to Polaron-Exciton Interactions. *ACS Appl. Mater. Interfaces* **2013**, *5* (17), 8733−8739.

(20) Lieb, M. A.; Zavislan, J. M.; Novotny, L. Single-Molecule Orientations Determined by Direct Emission Pattern Imaging. *J. Opt. Soc. Am. B* **2004**, *21* (6), 1210−1215.

(21) Kim, J.; Zhao, H.; Hou, S.; Khatoniar, M.; Menon, V.; Forrest, S. R. Using Fourier-Plane Imaging Microscopy for Determining Transition-Dipole-Moment Orientations in Organic Light-Emitting Devices. *Phys. Rev. Appl.* **2020**, *14* (3), 034048.

(22) Schuller, J. A.; Karaveli, S.; Schiros, T.; He, K.; Yang, S.; Kymissis, I.; Shan, J.; Zia, R. Orientation of Luminescent Excitons in Layered Nanomaterials. *Nat. Nanotechnol.* **2013**, *8* (4), 271−276.

(23) Jurow, M. J.; Morgenstern, T.; Eisler, C.; Kang, J.; Penzo, E.; Do, M.; Engelmayer, M.; Osowiecki, W. T.; Bekenstein, Y.; Tassone, C.; Wang, L.-W.; Alivisatos, A. P.; Brütting, W.; Liu, Y. Manipulating the Transition Dipole Moment of CsPbBr₃ Perovskite Nanocrystals for Superior Optical Properties. *Nano Lett.* **2019**, *19* (4), 2489−2496.

(24) Taminiau, T. H.; Karaveli, S.; van Hulst, N. F.; Zia, R. Quantifying the Magnetic Nature of Light Emission. *Nat. Commun.* **2012**, *3* (1), 979.

(25) Flämmich, M.; Frischeisen, J.; Setz, D. S.; Michaelis, D.; Krummacher, B. C.; Schmidt, T. D.; Danz, N.; Brütting, W. Oriented Phosphorescent Emitters Boost OLED Efficiency. *Org. Electron.* **2011**, *12* (10), 1663−1668.

(26) Kim, J.; Batagoda, T.; Lee, J.; Sylvinson, D.; Ding, K.; Saris, P. J. G.; Kaipa, U.; Oswald, I. W. H.; Omary, M. A.; Thompson, M. E.; Forrest, S. R. Systematic Control of the Orientation of Organic

Phosphorescent Pt Complexes in Thin Films for Increased Optical Outcoupling. *Adv. Mater.* **2019**, *31* (32), 1900921.

(27) Mak, K. F.; He, K.; Lee, C.; Lee, G. H.; Hone, J.; Heinz, T. F.; Shan, J. Tightly Bound Trions in Monolayer MoS2. *Nat. Mater.* **2013**, *12* (3), 207−211.

(28) Ross, J. S.; Wu, S.; Yu, H.; Ghimire, N. J.; Jones, A. M.; Aivazian, G.; Yan, J.; Mandrus, D. G.; Xiao, D.; Yao, W.; Xu, X. Electrical Control of Neutral and Charged Excitons in a Monolayer Semiconductor. *Nat. Commun.* **2013**, *4*, 1474.

(29) Berkelbach, T. C.; Hybertsen, M. S.; Reichman, D. R. Theory of Neutral and Charged Excitons in Monolayer Transition Metal Dichalcogenides. *Phys. Rev. B: Condens. Matter Mater. Phys.* **2013**, *88* (4), 045318.

(30) Kang, J.; Tongay, S.; Zhou, J.; Li, J.; Wu, J. Band Offsets and Heterostructures of Two-Dimensional Semiconductors. *Appl. Phys. Lett.* **2013**, *102* (1), 012111.

(31) Wang, Q.; Sun, B.; Aziz, H. Exciton-Polaron-Induced Aggregation of Wide-Bandgap Materials and Its Implication on the Electroluminescence Stability of Phosphorescent Organic Light-Emitting Devices. *Adv. Funct. Mater.* **2014**, *24* (20), 2975−2985.

(32) Gurarslan, A.; Yu, Y.; Su, L.; Yu, Y.; Suarez, F.; Yao, S.; Zhu, Y.; Ozturk, M.; Zhang, Y.; Cao, L. Surface-Energy-Assisted Perfect Transfer of Centimeter-Scale Monolayer and Few-Layer MoS$_2$ Films onto Arbitrary Substrates. *ACS Nano* **2014**, *8* (11), 11522−11528.

(33) Plechinger, G.; Nagler, P.; Kraus, J.; Paradiso, N.; Strunk, C.; Schüller, C.; Korn, T. Identification of Excitons, Trions and Biexcitons in Single-Layer WS$_2$. *Phys. Status Solidi RRL* **2015**, *9* (8), 457−461.

(34) Lu, H.; Kummel, A.; Robertson, J. Passivating the Sulfur Vacancy in Monolayer MoS$_2$. *APL Mater.* **2018**, *6* (6), 066104.

(35) Zeng, H.; Liu, G.-B.; Dai, J.; Yan, Y.; Zhu, B.; He, R.; Xie, L.; Xu, S.; Chen, X.; Yao, W.; Cui, X. Optical Signature of Symmetry Variations and Spin-Valley Coupling in Atomically Thin Tungsten Dichalcogenides. *Sci. Rep.* **2013**, *3* (1), 1608.

(36) Mouri, S.; Miyauchi, Y.; Matsuda, K. Tunable Photo-luminescence of Monolayer MoS2 via Chemical Doping. *Nano Lett.* **2013**, *13* (12), 5944−5948.

(37) Siviniant, J.; Scalbert, D.; Kavokin, A. V.; Coquillat, D.; Lascaray, J.-P. Chemical Equilibrium between Excitons, Electrons, and Negatively Charged Excitons in Semiconductor Quantum Wells. *Phys. Rev. B: Condens. Matter Mater. Phys.* **1999**, *59* (3), 1602−1604.

(38) Peimyoo, N.; Yang, W.; Shang, J.; Shen, X.; Wang, Y.; Yu, T. Chemically Driven Tunable Light Emission of Charged and Neutral Excitons in Monolayer WS$_2$. *ACS Nano* **2014**, *8* (11), 11320−11329.

(39) Amani, M.; Lien, D.-H.; Kiriya, D.; Xiao, J.; Azcatl, A.; Noh, J.; Madhvapathy, S. R.; Addou, R.; Kc, S.; Dubey, M.; Cho, K.; Wallace, R. M.; Lee, S.-C.; He, J.-H.; Ager, J. W.; Zhang, X.; Yablonovitch, E.; Javey, A. Near-Unity Photoluminescence Quantum Yield in MoS$_2$. *Science* **2015**, *350* (6264), 1065−1068.

(40) Forrest, S. R.; Bradley, D. D. C.; Thompson, M. E. Measuring the Efficiency of Organic Light-Emitting Devices. *Adv. Mater.* **2003**, *15* (13), 1043−1048.

(41) Coburn, C.; Lee, J.; Forrest, S. R. Charge Balance and Exciton Confinement in Phosphorescent Organic Light Emitting Diodes. *Adv. Opt. Mater.* **2016**, *4* (6), 889−895.

(42) Zhang, Y.; Lee, J.; Forrest, S. R. Tenfold Increase in the Lifetime of Blue Phosphorescent Organic Light-Emitting Diodes. *Nat. Commun.* **2014**, *5*, 5008.

(43) Celebi, K.; Heidel, T. D.; Baldo, M. A. Simplified Calculation of Dipole Energy Transport in a Multilayer Stack Using Dyadic Green's Functions. *Opt. Express* **2007**, *15* (4), 1762.